Nonlinear Dyn
https://doi.org/10.1007/s11071-024-10402-7

RESEARCH

Wideband vibration attenuation of a metamaterial beam via integrated hardening and softening nonlinear resonators

Jianlei Zhao · Ivana Kovacic · Rui Zhu

Received: 22 August 2024 / Accepted: 22 September 2024
© The Author(s), under exclusive licence to Springer Nature B.V. 2024

Abstract Nonlinear metamaterials (NLMs) have recently garnered significant interest for their abilities to achieve wide bandwidth in vibration attenuation and wave manipulation. However, NLMs proposed have been predominantly theoretical and conceptual due to nonlinearity being introduced through discrete spring models rather than the practically achievable components. To overcome this shortcoming, this paper proposes an original integrated design strategy leveraging a mono-slender beam configuration to tailor nonlinear stiffness and form quasi-linear, hardening and softening resonators. By adjusting only one geometric parameter of the beam, transitions between different nonlinear types can be realized. The nonlinear behaviors of resonators are verified through static force–displacement curves and frequency-amplitude responses. Subsequently, a metamaterial beam comprising a linear host beam and periodically distributed integrated hardening and softening nonlinear resonators is constructed. The dispersion relation for an infinite-size beam is derived using the transfer matrix method. The resulting complex band structure and nonlinear frequency response reveal that the bandgap is amplitude-dependent and more importantly, broadened due to the introduced nonlinearities. Furthermore, vibration attenuation in a finite NLM beam is demonstrated in a broad nonlinear-dependent frequency region which aligns well with the predicted bandgap. The analysis of the power spectral density within this region indicates that the attenuation is due to frequency dissipation caused by the nonlinear interaction between the resonators and the host beam. This study presents a promising solution for advancing the practical application of nonlinear metamaterials.

Keywords Nonlinear metamaterial · Wideband attenuation · Hardening nonlinearity · Softening nonlinearity · Integrated resonators

Abbreviations

A	Output root-time-square amplitude of the time domain
A_0	Initial excitation amplitude
$\Delta x,\Delta y$	End displacement in the x and y direction
$\delta x,\delta y$	Normalized displacement in the x and y direction
E,E_0	Young's modulus of hardening/softening beam and host beam
f_x,f_y,m_z	Normalized forces and moment in x and y directions and around z-axis

J. Zhao · R. Zhu (✉)
School of Aerospace Engineering, Beijing Institute of Technology, Beijing 100081, China
e-mail: ruizhu@bit.edu.cn

I. Kovacic
Faculty of Technical Science, Centre of Excellence for Vibro-Acoustic Systems and Signal Processing, University of Novi Sad, 21000 Novi Sad, Serbia

Published online: 14 October 2024

$f_h(y), f_s(y)$	Force–deflection characteristic of the hardening/softening nonlinear part
g_{ij}, p_{ij}, q_{ij}	Nondimensional beam characteristic coefficients
H	Transfer matrix for the NLM beam
I_0	Moment of inertia for the NLM beam
k_{h1},k_{s1}	Linear stiffness coefficients
k_{hi},k_{si}	Nonlinear stiffness coefficients
l	Beam length
l_c	Lattice constant of the periodic structure
m_j^1,m_j^2	Mass parameters for the j-th unit cell in the system
M_z	Moment in the z-direction
Q	Parameter capturing the beam's tilt influence
S_0	Cross-sectional area of the beam
t_0	Out-of-plane thickness of the beam
T	Vibration transmission
u_x, u_y,α	End displacements in the x and y directions and rotation angle
$W(x)$	Mode shape function
$W_j(x\prime)$	Mode function for the j-th unit cell
$\Phi(x)$	Shape function of the beam modes
$w(x,t)$	Transverse deflection of the beam
η	Degree of nonlinearity
θ	Initial angle between the beam's centerline and the vertical direction
v	Flexural wavenumber
ρ_0	Density of the material for host beam
ζ_h,ζ_s	Damping ratios for hardening and softening components
ω	Angular frequency
Ω_h,Ω_s	Non-dimensional excitation frequencies for hardening and softening components

1 Introduction

Research in science and engineering continuously focuses on overcoming the mechanical limitations of traditional materials and structures. Metamaterials, as engineered micro-structured materials with extraordinary properties, provide fresh insights and inspiration toward attaining this aim. Over the past several decades, metamaterials have been successfully applied to various fields, including vibration attenuation [1, 2], cloaking devices [3, 4], superlenses [5, 6], negative refraction [7], and directional waveguide [8, 9].

Metamaterials also offer an effective way to manipulate wave propagation and vibration through their frequency bandgap, which controls wave propagation. A notable subset of these metamaterials is locally resonant (LR) metamaterials, designed to suppress wave propagation in low-frequency ranges, overcoming the limitations of Bragg scattering. Consequently, this innovation has led to the development of practical meta-beams [10, 11], meta-plates [12, 13], and meta-surfaces [14] capable of suppressing elastic wave and vibration propagation. The majority of current designs of locally resonators exhibit linear dynamic behavior, represented by mass-membrane [15, 16], mass-rubber [17], mass-screws [18], beam-type [19, 20], plate-type [21, 22] structures and piezoelectric transducers [23, 24] with electrical shunting.

However, due to their inherently linear resonance mechanisms, their effective bandwidth is narrow. In contrast, nonlinear dynamic characteristics not only widen the bandwidth but also introduce new mechanism, revealing interesting wave propagation phenomena absent from linear metamaterials (LMs), such as harmonic generations [25], dispersion modulation [26, 27], amplitude-dependent bandgaps [28–30], nonreciprocal wave propagation [31], and solitary waves [32, 33].

Recent endeavors to analyze elastic wave propagation in nonlinear metamaterials still utilize mass-spring chain systems or continuous linear host structure with array of distributed 1-DOF virtual nonlinear mass-spring absorbers. These studies emphasize the importance of introducing nonlinearity in periodic chains on wave propagation and attenuation, demonstrating nonlinear modeling methods form a theoretical perspective. For example, Narisetti et al. [34] analyzed frequency-dispersion shifts in nonlinear monoatomic chain with hardening and softening nonlinear using perturbation method. Manktelow et al. [35] used a multiple scales method to study the wave-wave interactions in similar system. In [36], the feasibility of employing a purely nonlinear mass-in mass system as unit cells for broad bandwidth metamaterial was explored. Yu et al. [37] numerically analyzed the wave attenuation in a 1D metamaterial with different nonlinear subunits. Fang et al. [38] demonstrated that large amplitudes in strongly

nonlinear triatomic chains could widen the bandgap. Shen et al. [39] focused on 1D metamaterial beams with embedded nonlinear resonators exhibiting softening or hardening cubic nonlinearity. Their study demonstrated that these nonlinearities can significantly enhance the bandgap width. Additionally, Shen et al. [40] further investigated 2D metamaterial honeycombs with periodically distributed nonlinear resonators designed in a spider web-like configuration. This research shows how the nonlinearities, whether softening or hardening, can be optimized to significantly enhance the bandgap width. Our previous work [41] proposed an ultra-broad bandgap strategy induced by combining hardening and softening nonlinearity in a triatomic chain, showing that the bandgap could be more than twice as wide as in the corresponding linear case. Casalotti et al. [42] proposed a metamaterial beam with periodic distributed nonlinear 1-DOF mass-spring absorbers, significantly reducing vibration associated with the lowest three vibration modes. Xu et al. [43] combined nonlinearity and damping effects in a metamaterial beam to achieve a broad bandgap. Zhou et al. [44] designed a metamaterial beam with embedded quasi-zero stiffness resonators, achieving a wide low-frequency bandgap. Fang [45] studied a vibro-impact resonator periodically attached to the host beam and showed a novel regime called chaotic band that can broaden the bandgap for low-frequency waves. Xia et al. [46] focused on metamaterial beams with bistable resonators, enhancing bandwidth through amplitude-dependent nonlinear inter-well oscillations. Wang et al. [47] proposed a multi-scale material integrated into a nonlinear metamaterial beam for whole-band vibration absorption across low, medium, and high-frequency ranges by replacing the mass components with composite mass bodies filled with microscopic particles.

These endeavors have proven that, when compared to LMs, nonlinearity provide new approaches to widen band gaps and enrich wave propagation phenomena. However, the introduction of nonlinear dynamic behavior through theoretical discrete spring models rather than real, physically realizable components implies that nonlinear metamaterials remain largely theoretical and conceptual. From a practical application perspective, nonlinear metamaterials need to be designed and fabricated from the resonator level to the metamaterial level to enable one to realize the proposed nonlinear dynamic characteristic practically. Although several applications have been reported in vibration energy harvesting [48, 49], vibration isolation [50, 51], and shock absorption [52], where nonlinearity is realized using combinations of linkages [53], an X-shaped structure [54, 55], and magnets [56]. Moreover, Vakakis et al. [57] showed that through purely geometric effects it is possible to achieve transitions from hardening to softening nonlinearity in an single degree of freedom oscillator composed of multiple stiffness elements. Fan et al. [58] presented a novel design of nonlinear magnetic mass-beam resonators capable of exhibiting hardening or softening nonlinearities. Their work, which includes both theoretical and experimental investigations, reveals tunable band gaps. Furthermore, Shen et al. [59] proposed metamaterial lattices embedded with piezoelectric membrane-shaped nonlinear resonators, demonstrating the potential of such resonators to maximize the bandgap width and adaptability. Li et al. [60] proposed a nonlinear pendulum metamaterial capable of realizing an ultra-low-frequency field effect bandgap. These designs of nonlinear metamaterials often involve multiple mechanical components, which can result in resonators that are less robust and compact, posing significant challenges for their direct use in metamaterials. To address these issues, only a few recent research has been increasingly focusing on the development of structurally integrated design approaches for nonlinear resonators. Zhao et al. [61] introduced a nonlinear damped metamaterial capable of achieving wideband vibration attenuation by integrating inertia amplifiers as nonlinear local resonators into a linear host structure. Yu et al. [62] proposed nonlinear metamaterial beam embedded with Kresling origami configuration under large deformations and demonstrate the emergence of unique frequency components resulting from nonlinear coupling stiffness.

An integrated structural design strategy that allows for the customization of nonlinear stiffness characteristics holds significant promise for advancing the practical use of nonlinear metamaterials. In this study, we present a novel approach using a mono-slender beam configuration that achieves the desired nonlinear force–displacement behavior. The proposed beam configuration is mechanically robust due to its simplicity, as it comprises only a few beam components. This design is also extremely compact, reliable, and efficient in terms of minimal space and weight constraints. By changing one geometric parameter

only, different qualitative and quantitative shapes of the force–displacement curve, and thus the nonlinear stiffness, can be effectively realized. This includes quasi-linear, weak hardening, Duffing hardening, softening, quasi-zero, and bistable characteristics. This work, therefore, provides a significant step forward in the design of compact, robust, and efficient nonlinear metamaterial systems.

Following this introduction and extending our previous work [41] on broad bandgap creation through combined hardening and softening nonlinearities in triatomic mass-spring chains, Sect. 2 presents a conceptual model of metamaterial beam with integrated hardening and softening nonlinear resonators, accompanied with its Euler–Bernoulli beam-based mathematical modelling. It further elucidates the transition strategy from hardening to softening nonlinearity in a mono-slender beam, providing designers with a powerful tool to characterize both hardening and softening nonlinearities. The proposed designs are theoretically verified through static force–displacement curves and dynamic amplitude-frequency response curves. Section 3 investigates the propagation of flexural waves in such a metamaterial beam using the transfer matrix method based on the Floquet-Bloch theorem. Section 4 numerically verifies the wideband vibration attenuation due to hardening and softening nonlinearity. Section 5 draws the conclusion of this work.

2 Modeling of the NLM beam

2.1 Conceptual model

Schematic of the proposed NLM beam is shown in Fig. 1a. It comprises a host beam and periodically attached hardening and softening resonators. The host beam undergoes linear deformation, while nonlinearity is introduced through the attached resonators. As depicted in Fig. 1b, each resonator consists of both a hardening and softening nonlinear component. The hardening nonlinearity is achieved via the large deformation of four parallel flat beams, while the softening nonlinearity is generated from the large deformation of four oblique beams. The mass m_1 is the connecting structure (green frame) between the beams, while the mass m_2 is orange center mass connecting the four oblique beams.

Consequently, the resonator unit can be modeled as a nonlinear spring-mass resonator with two degrees of freedom, i.e. with two spring-mass oscillators arranged in series. The equivalent mechanical model of the finite metamaterial beam, featuring an array of periodically arranged nonlinear hardening and softening spring-mass resonators, is shown in Fig. 1c. This model can be utilized subsequently to analyze the propagation of flexural waves in the NLM beam using the transfer matrix method based on the Floquet-Bloch theorem.

2.2 The hardening–softening transition in the nonlinear response of a fixed-guided beam

It has been demonstrated that the nonlinear response of a beam significantly depends on its geometric configuration and the type of boundary condition being imposed [63–65]. Typically, the load–deflection characteristic of a doubly clamped beam can be modeled as a Duffing hardening spring. Mettler [66] first recognized that for axially restrained beams, the dominant nonlinearity arises from the axial stretching, with curvature-induced nonlinearity being negligible. Therefore, this work aims to develop an efficient method to intentionally tune the axial stretching through different initial angle configurations, which provides a powerful tool for the designers to achieve hardening or softening nonlinearities. Figure 2a illustrates the nonlinear deflections of a fixed-guided beam at three initial angle configurations. The normalized force–displacement relationship is expressed as $\widehat{f}_i - \widehat{y}$, where $\widehat{f}_i = f_i/\max(f_i)$ and $\widehat{y} = y/l$. By choosing different initial angle θ between the beam's centerline and the vertical direction, we show that it is possible to tune the axial strength level and therefore, achieve the hardening–softening transition in the beam's nonlinear deflection results. When the angle θ increases, a transition can be observed from hardening nonlinearity to softening nonlinearity and eventually turn to a bistable type with negative stiffness. So, there are three cases considered: Case (i), with $\theta < \pi/2$, Case (ii), with $\theta = \pi/2$, and Case (iii), with $\theta > \pi/2$. Specifically, Case (ii) is similar to the half-symmetry case of the doubly clamped beam and therefore, the force–displacement relationship exhibits Duffing hardening nonlinearities, as seen in

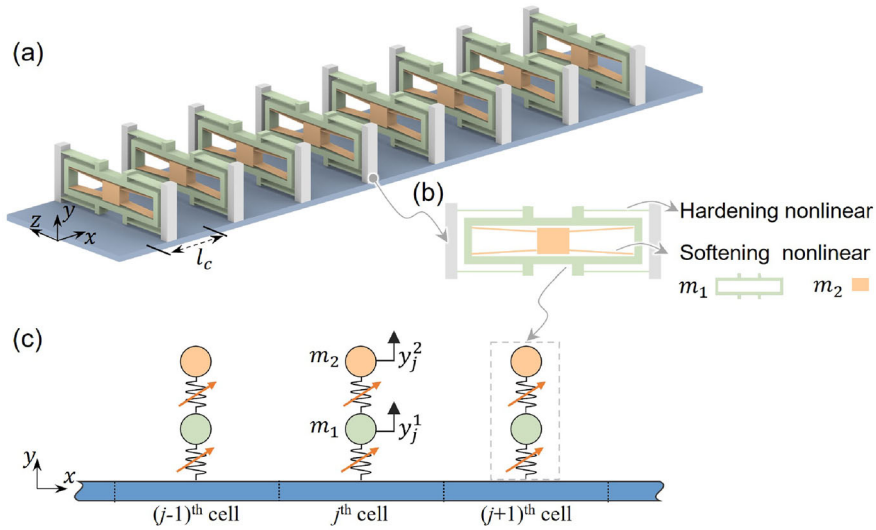

Fig. 1 **a** Schematic of a finite metamaterial beam with attached hardening and softening nonlinear resonators, **b** Hardening and softening nonlinear resonators as continuous elements, **c** Equivalent mechanical model of the finite metamaterial beam with an array of periodic hardening and softening nonlinear spring-mass resonators arranged in series

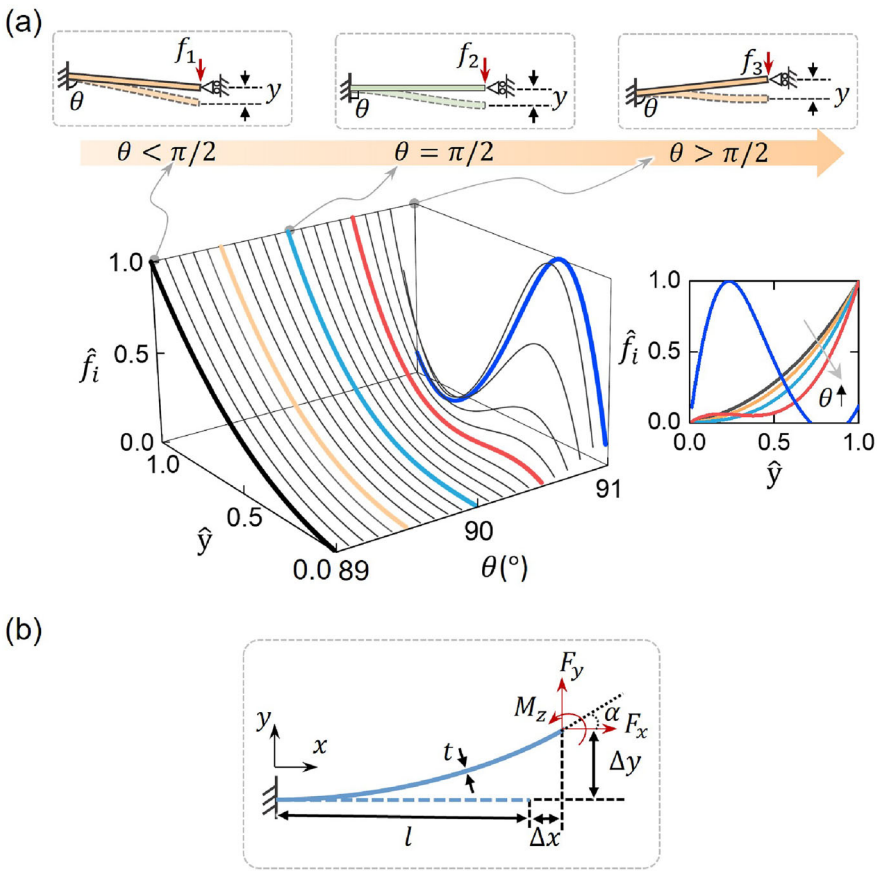

Fig. 2 **a** Three cases showing different initial angles θ of a fixed-guided beam and their corresponding normalized load–deflection schematic diagrams. Case (i): $\theta < \pi/2$, Case (ii): $\theta = \pi/2$, Case (iii): $\theta > \pi/2$; **b** (**a**) Generalized flexible beam

Fig. 2a. Case (i) is an initially downward-inclined beam configuration, which produces less axial stretching than that produced by the flat beam configuration in Case (ii) and therefore, mainly provides hardening nonlinearity, but the hardening strength is weaker than Case (ii). In Case (iii), the axial stretching starts at a

negative value (the beam is compressed initially) and then changes to positive values, which is similar to a buckled configuration that enables the realization of softening nonlinearity. Thus, the ability to transition between hardening and softening responses through simple geometric adjustments (changing θ) in a fixed-guided beam provides significant design flexibility for targeting specific nonlinearities. Additionally, this approach can be easily implemented in the fabrication process.

The nonlinear static properties of various geometric initial angle configurations can be derived using the Beam-Constraint Model (BCM) [67]. The BCM has been proven to accurately capture the large deflections of flexible beams in compliant mechanisms. Additionally, the BCM is simple, parametric, and provides closed-form solutions.

Figure 2b illustrates a generalized flexible beam in its undeformed and deformed states with end-loads F_x, F_y, M_z and end displacements Δx, Δy, α. These loads and displacements are normalized with respect to the beam parameters and are given by the following expressions:

$$f_x = \frac{F_x l^2}{EI}, f_y = \frac{F_y l^2}{EI}, m_z = \frac{M_z l^2}{EI}, \delta_x = \frac{\Delta x}{l}, \delta_y = \frac{\Delta y}{l} \tag{1}$$

where I represents the moment of inertia of the rectangular section, and E and t represent the Young's modulus and thickness of the beam, respectively. The BCM characterizes the load–deflection relationships of the beam through the following parametric and closed-form equations:

$$\begin{bmatrix} f_y \\ m_z \end{bmatrix} = \begin{bmatrix} g_{11} & g_{12} \\ g_{21} & g_{22} \end{bmatrix} \begin{bmatrix} u_y \\ \alpha \end{bmatrix} + f_x \begin{bmatrix} p_{11} & p_{12} \\ p_{21} & p_{22} \end{bmatrix} \begin{bmatrix} u_y \\ \alpha \end{bmatrix} + f_x^2 \begin{bmatrix} q_{11} & q_{12} \\ q_{21} & q_{22} \end{bmatrix} \begin{bmatrix} u_y \\ \alpha \end{bmatrix} \tag{2}$$

$$u_x = \frac{t^2 f_x}{12} - \frac{1}{2} \begin{bmatrix} u_y, \alpha \end{bmatrix} \begin{bmatrix} p_{11} & p_{12} \\ p_{21} & p_{22} \end{bmatrix} \begin{bmatrix} u_y \\ \alpha \end{bmatrix} - f_x \begin{bmatrix} u_y \alpha \end{bmatrix} \begin{bmatrix} q_{11} & q_{12} \\ q_{21} & q_{22} \end{bmatrix} \begin{bmatrix} u_y \\ \alpha \end{bmatrix} \tag{3}$$

In these equations, the coefficients g_{ij}, p_{ij} and q_{ij} ($i,j = 1, 2$) are nondimensional beam characteristic coefficients listed in Table 1, as provided in the referenced source [67].

To more accurately capture the large deflection behavior of the beam, each configuration shown in Fig. 2a can be divided into several elements, with each element modeled sequentially by the BCM. This process, known as the Chain Beam-Constraint Model (CBCM) [68], allows for the calculations of the force–displacement nonlinear relations of the beam by applying the BCM equations to each element and incorporating the boundary constraints.

2.3 Design of the hardening nonlinear resonator

As depicted in Fig. 3a, the hardening nonlinear component consists of four clamped flat beams. Due to the structured symmetry of the resonator unit cell, each of these beams can be modeled as Case (ii) in Fig. 2a. Consequently, the load–deflection characteristic of the hardening nonlinear part can be expressed as:

$$f_{\mathrm{h}}(y) = 4f_2 \tag{4}$$

where f_2 is obtained using the CBCM method described in Sect. 2.1.

With the parameters $l = 40mm, t = 0.025 * l$, beam width $b = 10mm$, and Young's modulus $E = 194 \times 10^9 Pa$, the force–displacement curve obtained via CBCM is plotted in Fig. 3b. A finite element (FE) analysis was also conducted using the commercial FE software ANSYS. In this analysis, the beam part was modeled using the Beam 189 element type, while the remaining part was modeled using the Plane 182 element with a large modulus of elasticity to simulate a rigid body mass. The force–displacement curves obtained from the FE analysis are shown as a dashed line in Fig. 3b, demonstrating good agreement with the CBCM results.

The force–displacement characteristic can be modeled by a hardening Duffing spring as: $f_h = k_{h1} y_h + k_{h3} y_h^3$. The dimensionless displacement is defined as $\widehat{y}_h = y_h / l$. The Duffing fitting result is plotted as hollow circles in Fig. 3b. We notice that the elastic force can be divided into two components: a linear term due to the bending and a nonlinear term due to the axial stretching. This division has been reasonably demonstrated in the design of hardening Duffing energy harvesters [65]. Therefore, by varying the ratio of bending strain to stretching strain, the nonlinear term can be intentionally designed. The

Table 1 The nondimensional characteristic coefficients of the BCM matrices

g_{11}	$g_{12}=g_{21}$	g_{22}	p_{11}	$p_{12}=p_{21}$	p_{22}	q_{11}	$q_{12}=q_{21}$	q_{22}
12	− 6	4	6/5	− 1/10	2/15	− 1/700	1/1400	− 11/6300

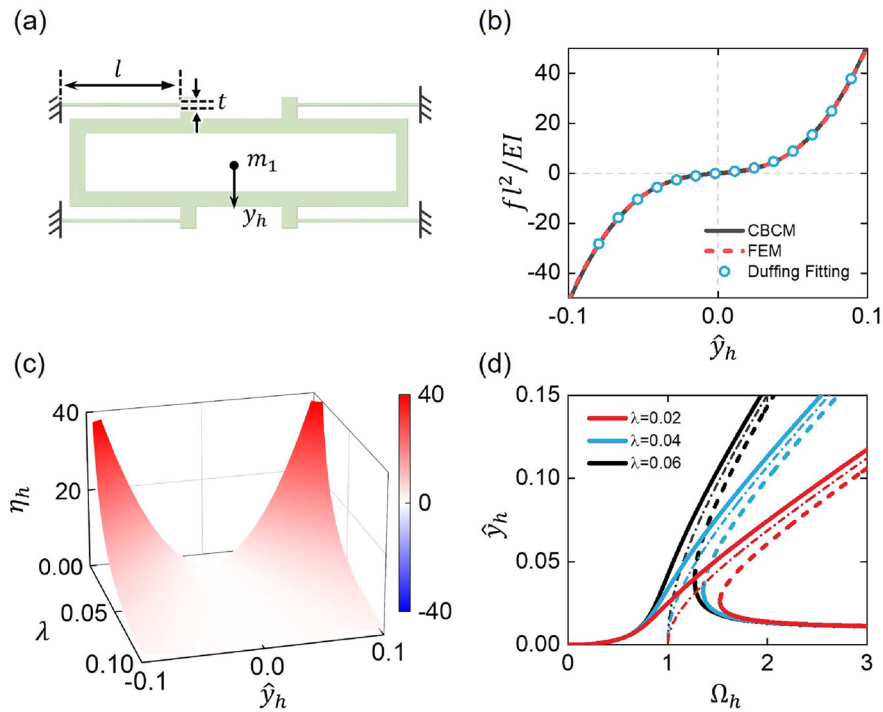

Fig. 3 **a** Hardening nonlinear resonator, **b** Hardening nonlinear force–displacement verification case; **c** The influence of slenderness ratio and excitation amplitude on the degree of nonlinearity, **d** Nonlinear dynamic response of the equivalent dynamic model of resonator cell with different slenderness ratios

slenderness ratio of the beam is a critical parameter affecting this variation of the ratio of the bending strain and stretching strain and therefore, further affects the degree of nonlinearity. The slenderness ratio is defined as $= t/l$. The degree of nonlinearity η is defined as the ratio of the nonlinear stiffness term to the linear stiffness term. For a hardening Duffing nonlinear system, this parameter η is defined as: $\eta_{\mathrm{h}} = \frac{3k_{h3}y_h^2}{k_{h1}}$ where $\eta_{\mathrm{h}} > 0$ indicates stiffness hardening and $\eta_{\mathrm{h}} < 0$ indicates stiffness softening. Figure 3c illustrates the effect of the slenderness ratio on the degree of nonlinearity. First, it is evident that the degree of nonlinearity increases as the slenderness ratio decreases for the same level of excitation. Consequently, the corresponding backbone curve and the amplitude-frequency branches bent downwards, yielding the lower amplitude for smaller slenderness ratios. Theoretically, for a quasi-zero thickness beam ($\lambda \approx 0$), one has that the linear stiffness$k_{h1} \approx 0$. In this scenario, the static characteristic resembles a tensioned wire, where only axial stretching deformation is considered, not bending deformation.

To quantify the design hardening nonlinearity, the hardening nonlinear component shown in Fig. 3a can be simplified to a single degree of freedom Duffing oscillator under base excitation. The multiple scales method [69] was used to solve the frequency response curves of the hardening nonlinear resonator. The derivation procedure according to the standard multiple scales method is detailed in Appendix A1. In Fig. 3d, we illustrate the effect of varying the slenderness ratio λ on the frequency hardening with a constant excitation amplitude $\hat{y}_{h0} = 0.01$. When the slenderness ratio λ increases, a noticeable reduction in the leaning tendency toward higher frequencies can be found, indicating that the hardening nonlinearity decreases. Conversely, when the slenderness ratio λ

decreases, the hardening nonlinearity increases. This relationship paves the way for achieving the designable nonlinearity at small-amplitude vibration via the beam's slenderness ratio tuning.

2.4 Design of the softening nonlinear resonator

As analyzed in Sect. 2.1, introducing a buckled configuration can lead to the stiffness softening. Thus, by adjusting the initial configuration angle of the beam, we show that it is possible to achieve the softening response. The equivalent softening spring design requires symmetrical reciprocating motion at the equilibrium position, implying a symmetrical static response. Therefore, a symmetrically structural design is essential. As shown in Fig. 4a, the softening nonlinear component consists of a pair of beams from Case (i) and a pair of beams from Case (iii), resulting in a symmetrical configuration. The load–deflection characteristic of the softening nonlinear part is expressed as:

$$f_s(y) = 2(f_1 + f_3) \tag{5}$$

where f_1 and f_3 can be obtained using the CBCM method described in Sect. 2.1.

With the parameters$t = 0.005 * l, \theta = 93^{\circ}$, and other parameters being consistent with those of the hardening part, the corresponding force–displacement curve obtained by CBCM is plotted in Fig. 4b. The slope of the curve decreases, indicating softening stiffness. Additionally, the force–displacement curve obtained from FEA and polynomial fitting results are also plotted in Fig. 4b, showing a good agreement. Different from the hardening Duffing fitting, the softening force–displacement characteristic is fitting by the polynomials as $f_s = \sum_{i=1}^{n} k_{si} {y_s}^i$ $(n = 8)$. The dimensionless displacement is defined as$\hat{y}_s = y_s/l$. To gain deeper understanding of the full potential of the initial configuration angle design on the resulting nonlinear type, we further consider the combined influence of the slenderness ratio and the initial configuration angle on the corresponding nonlinear response. Hence, we introduce the parameter of interest $Q = \frac{|\cos\theta|}{\lambda}$, to quantitatively capture this influence. It is worth noting that Q represents the ratio of the span height of the oblique beam to the thickness of the beam. A higher Q indicates a greater tilt of the beam. Similar to the hardening nonlinear case, the degree of nonlinearity η is defined as the ratio of the nonlinear stiffness term to the linear stiffness term,

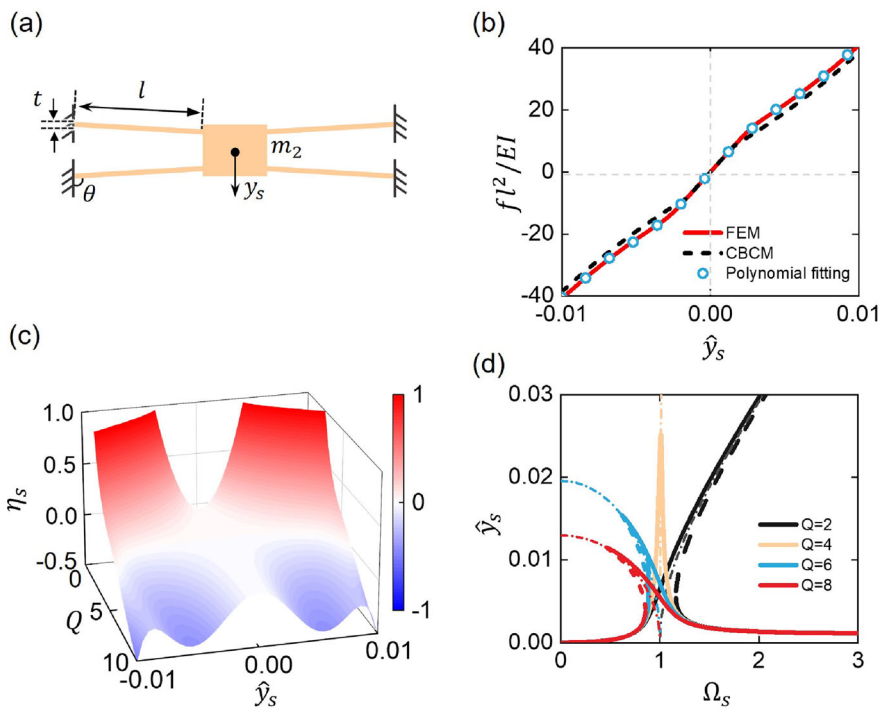

Fig. 4 **a** Softening nonlinear resonator, **b** Softening nonlinear force–displacement verification case; **c** The influence of the parameter Q and excitation amplitude on the degree of nonlinearity, **d** Nonlinear dynamic response of the equivalent dynamic model of resonator cell with different Q

as $\eta_s = \frac{\sum_{i=2}^{n} i k_{si} y_s^{i-1}}{k_{s1}}$. It is also noteworthy that $\eta_s > 0$ means hardening stiffness, while $\eta_s < 0$ means softening stiffness. As shown in Fig. 4c, as Q increases, an apparent transition from hardening to softening effects is seen. More explicitly, to achieve a softening nonlinear type, Q must exceed a certain threshold. Otherwise, the system remains hardening nonlinear. Furthermore, we investigate this transition by simplifying the softening part in Fig. 4a to an equivalent single degree of freedom oscillator. The equivalent spring is determined by the fitting polynomial mentioned earlier. The fundamental mode frequency response for this polynomial nonlinear type can be solved using the multiple scales method [69]. The derivation procedure is detailed in Appendix A2. As illustrated in Fig. 4d. By varying the parameter Q and with a constant excitation amplitude $\widehat{y}_{s0} = 0.001$, the transition from nonlinear hardening to softening is clearly depicted. Specifically, as Q changes from $Q = 2$ to $Q = 4$, the hardening nonlinearity weakens to an approximately linear type of the response. As Q increases from $Q = 4$ to $Q = 8$, the softening nonlinearity becomes more apparent.

3 Propagation of flexural wave in NLM beam

3.1 Dispersion relation by transfer matrix method

In this section, we study the dispersion of the NLM beam with nonlinear resonators. The host beam is modeled using the Euler–Bernoulli beam assumption, governed by

$$E_0 I_0 \frac{\partial^4 w(x,t)}{\partial x^4} + \rho_0 S_0 \frac{\partial^2 w(x,t)}{\partial t^2} = 0 \tag{6}$$

where w is the transverse deflection of the beam, E_0, I_0, ρ_0, S_0 are the elastic modulus, moment of inertia, density, and cross-section area, respectively.

Assuming the transverse deflection of the beam as

$$w(x) = W(x)\mathrm{e}^{\mathrm{i}\omega t} \tag{7}$$

where ω is the angular frequency and $W(x) = \mathbf{\Delta}\mathbf{\Phi}(x)^{\mathrm{T}}$ is the mode shape function, with:

$$\mathbf{\Delta} = \{\, A \quad B \quad C \quad D \,\} \tag{8}$$

$$\mathbf{\Phi}(x) = \{\, \cos(vx) \quad \sin(vx) \quad \cosh(vx) \quad \sinh(vx) \,\} \tag{9}$$

where A, B, C, D are unknown coefficients, v is the flexural wavenumber and the dispersion relation of the bare beam without resonators can be expressed as $v^4 = \frac{\rho_0 S_0}{E_0 I_0}\omega^2$. In the j$^{\text{th}}$ unit cell where $x\prime = x - jl_{\mathrm{c}}$ and $jl_{\mathrm{c}} \le x \le (j+1)l_{\mathrm{c}}$ and l_{c} is the lattice constant, the mode function can be written as $W_j(x\prime) = \Delta_j \Phi(x\prime)^{\mathrm{T}}$, where $\mathbf{\Delta}_j = \{\, A_j \quad B_j \quad C_j \quad D_j \,\}$.

The governing equation of motion for the resonator can be written down as follows

$$\begin{aligned} &m_j^1 \ddot{y}_j^1 + k_{\mathrm{h1}}(y_j^1 - w(x_j,t)) + k_{\mathrm{h3}}(y_j^1 - w(x_j,t))^3 \\ &\quad + k_{\mathrm{s1}}(y_j^1 - y_j^2) + \sum_{i=2}^{n} k_{si}(y_j^1 - y_j^2)^i \\ &\quad = 0 \end{aligned} \tag{10}$$

$$m_j^2 \ddot{y}_j^2 + k_{\mathrm{s1}}(y_j^2 - y_j^1) + \sum_{i=2}^{n} k_{si}(y_j^2 - y_j^1)^i = 0 \tag{11}$$

We consider only fundamental wave propagation and, thus, it is assumed that

$$y_j^1 = \big(W_j(0) + Y_1\big)\mathrm{e}^{\mathrm{i}\omega t} + cc. \tag{12}$$

$$y_j^2 = (W_j(0) + Y_1 + Y_2)\mathrm{e}^{\mathrm{i}\omega t} + cc. \tag{13}$$

where Y_1 is the motion amplitude of mass m_1 relative to the connection point, and Y_2 is the motion amplitude of mass m_2 relative to m_1. By substituting Eqs. (12–13) into Eqs. (10–11), and using the multiple scales method to this polynomial nonlinear system, we obtain

$$\begin{aligned} &-(m_j^1 + m_j^2)\omega^2\big(W_j(0) + Y_1\big) + k_{\mathrm{h1}}Y_1 + 3/4k_{\mathrm{h3}}Y_1^3 \\ &\quad - m_j^2\omega^2 Y_2 = 0 \end{aligned} \tag{14}$$

$$\begin{aligned} &-m_j^2\omega^2\big(W_j(0) + Y_1 + Y_2\big) + k_{\mathrm{s1}}Y_2 - 5/6k_{\mathrm{s2}}^2 Y_2^3 \\ &\quad + 3/4k_{\mathrm{s3}}Y_2^3 = 0 \end{aligned} \tag{15}$$

The derivation procedure is detailed in Appendix A3. These two equations can be used to obtain the amplitudes Y_1 and Y_2.

Considering the continuities of the displacement, slope, bending moment and shear force at the attaching point of the resonator, and employing the Floquet-Bloch theorem $\mathbf{\Delta}_j = \mathrm{e}^{\mathrm{i}ql_{\mathrm{c}}}\mathbf{\Delta}_{j-1}$ and the transfer matrix

method, the dispersion relation of the NLM beam can be derived as

$$\left|\mathbf{G}^{-1}\mathbf{H} - \mathrm{e}^{\mathrm{i}ql_c}\mathbf{I}\right| = 0 \tag{16}$$

where $\mathbf{I}$ is the identity matrix, q is the bending wave vector, and $\mathbf{H}$ and $\mathbf{G}$ from Eq. (16) are defined by

$$\mathbf{H} = \begin{bmatrix} \cos(vl_c) & \sin(vl_c) & \cosh(vl_c) & \sinh(vl_c) \\ -v\sin(vl_c) & v\cos(vl_c) & v\sinh(vl_c) & v\cosh(vl_c) \\ -v^2\cos(vl_c) & -v^2\sin(vl_c) & v^2\cosh(vl_c) & v^2\sinh(vl_c) \\ EIv^3\sin(vl_c) & -EIv^3\cos(vl_c) & EIv^3\sinh(vl_c) & EIv^3\cosh(vl_c) \end{bmatrix} \tag{17}$$

$$\mathbf{G} = \begin{bmatrix} 1 & 0 & 1 & 0 \\ 0 & v & 0 & v \\ -v^2 & 0 & v^2 & 0 \\ g_{41} & -EIv^3 & g_{43} & EIv^3 \end{bmatrix} \tag{18}$$

where

$$g_{41} = g_{43} = \frac{-\left(m_j^1\omega^2\left(W_j(0) + Y_1\right) + m_j^2\omega^2\left(W_j(0) + Y_1 + Y_2\right)\right)}{W_j(0)} \tag{19}$$

Strictly speaking, the Floquet-Bloch theorem cannot be applied to nonlinear periodic systems, and a recent review [70] of nonlinear metamaterials provides a detailed discussion for the applicability of Bloch's theorem. In our study, the nonlinearity is localized within the constitutive properties of the local resonators. Perturbation techniques allow the nonlinear field equations to be approximated by a hierarchy of linear equations, enabling a reasonable application of Floquet-Bloch conditions for analyzing dispersion features in nonlinear periodic systems.

For a given frequency, the wave vector solution can be obtained from the dispersion relation. In the special case where $k_{hi} = k_{si} = 0, (i > 2)$, Eq. (16) degenerates into the linear dispersion relation.

3.2 The frequency responses and bandgap structure

The effects of nonlinearity of the attached resonator unit on the frequency band structure, particularly on the widths of the bang gaps, are investigated as illustrated in Fig. 5. Here, the parameters are set as follows: the lattice constant $l_c = 60mm$, Young modulus $E_0 = 70 \times 10^9$Pa, the density $\rho_0 = 2700\text{kg/m}^3$, the thickness of the beam $t_0 = 2$mm, the out-of-plane thickness $b_0 = 128$mm. The geometric parameters of the hardening beam and the softening beam are the same as those in Figs. 3b and 4b respectively. The mass parameters $m_1 = 0.385 \times 10^{-1}$kg and $m_2 = 0.086 \times 10^{-1}$kg.

First, the linear case was considered as having the same constant linear spring stiffness coefficients as the attached resonator. As shown in Fig. 5a–b, two resonant modes are identified in the frequency response of the attached resonator. Furthermore, each resonant mode frequency generates a bandgap, as predicted by both the imaginary and real parts in Fig. 5c–d.

For the nonlinear cases, the effects of the excitation amplitude are examined. It is observed that in the amplitude-frequency curve of mass m_1 shown in Fig. 5a, there is the antiresonance between two distinctive resonances, while in the amplitude-frequency curve of mass m_2 shown in Fig. 5b, there is a well between them, which descends and flattens toward 0 dB. The first-resonance branches bend toward lower frequencies, corresponding to the softening behaviour, while the second-resonance branches exhibit multiple bending: first towards lower frequencies and then towards higher frequency, implying the mixed softening-hardening type of the behaviour [71]. The degree of this bending increases with the excitation amplitude.

The complex bandgap structure is particularly intriguing, as depicted in Fig. 5c–d. For real parts, similar to the amplitude-frequency curves, frequency-real-wavevector curves lean toward lower or higher frequencies, resulting in multiple values of real wavevector corresponding to certain frequencies. It is noted that the actual possible frequency-wavevector depends on the stable amplitude-frequency responses. The imaginary part can directly characterize the wave attenuation characteristics and the bandgap region, so it can more clearly reflect the effects of nonlinear and excitation amplitude on the bandgap. In Fig. 5c, d, the grey shaded area represents the bandgap region for linear case. For nonlinear case, the high frequency branch corresponding to the second band gap bends toward lower frequencies, causing the second bandgap to extend to lower frequencies and approach the first bandgap. Explicitly, as the excitation amplitude increases, this extension becomes more apparent. Additionally, the low frequency branch corresponding

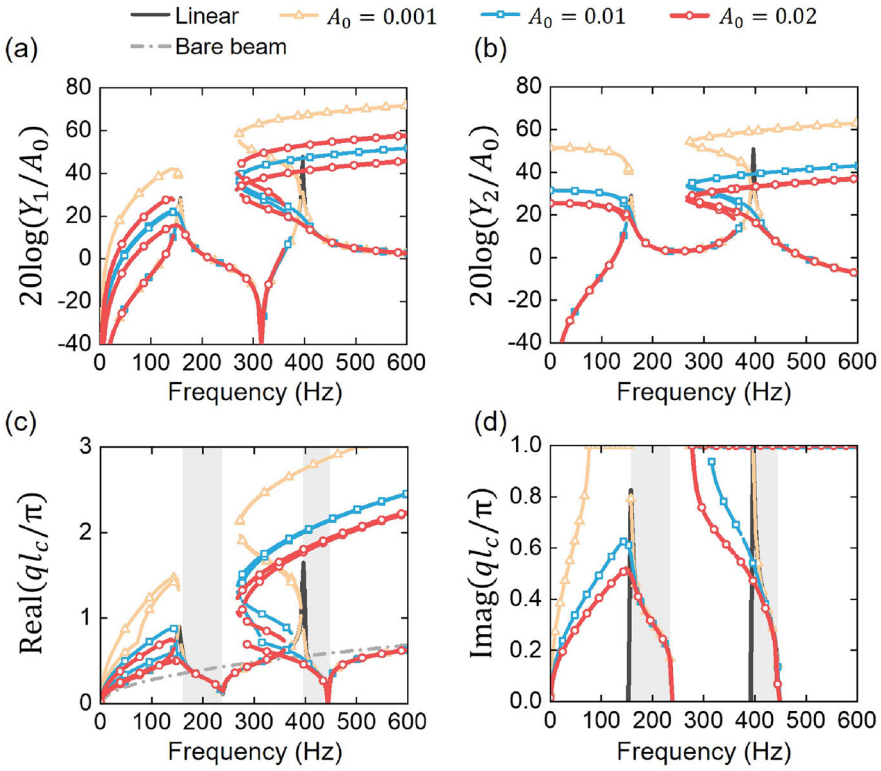

Fig. 5 **a** Amplitude-frequency response of mass m_1 for different excitation amplitudes, **b** Amplitude-frequency response of mass m_2 for different excitation amplitudes, **c** Real part of bandgap structure for different excitation amplitudes. **d** Imaginary part of bandgap structure for different excitation amplitudes

to the first band gap bends toward a zero-frequency value, which seem to reflect a bandgap starting at zero frequency. However, we point out that, essentially, this apparent zero-frequency bandgap is misleading, as the new emerging imaginary branch starts from zero frequency results from an unstable amplitude-frequency curve. This is further evident by numerical calculations of wave propagation in NLM beam in the following Sect. 4.

4 Numerical verifications

To further validate our analytical results, FE simulations were conducted. As illustrated in Fig. 6a, an NLM beam with a finite length consisting of 8 resonator units with free-free boundary condition was modeled in ANSYS. The relevant geometry, material and mass parameters are consistent with those in Sect. 3.2. An external sinusoidal excitation $\omega_{in} = A_0 \sin\omega t$ was applied on the left-band side of the beam. The simulation utilized 8-node Solid185 element type, and a mesh convergence analysis was performed out to ensure the adequate numerical accuracy. The mesh details of the attached resonator are shown in Fig. 6b.

A time-domain nonlinear transient analysis was conducted to obtain the time transient displacement for the nonlinear case. By maintaining constant frequency and amplitude of excitation for 100 periods, the transient oscillations dissipate, resulting in steady-stable periodic motion. The time step was fixed at 1/20 of the excitation period. Therefore, 20,000 calculation steps are required for each excitation frequency. This made the computation of a single transmissibility curve extremely time-consuming. To reduce the calculation time, as shown in Fig. 6c, the beam structure was modeled using the Beam189 element type, and the corresponding mass body was modeled by the Mass21 element type. The remaining connection parts were treated as rigid connection and modeled using node coupling technology in ANSYS. Specifically, the node-coupled sets for connections were defined as follows: CP1 for the main beam-to-hardening beam, CP2 for the hardening beam-to-m_1-to-softening beam, CP3 for the softening beam-to-m_2. This beam element-dominated modeling method

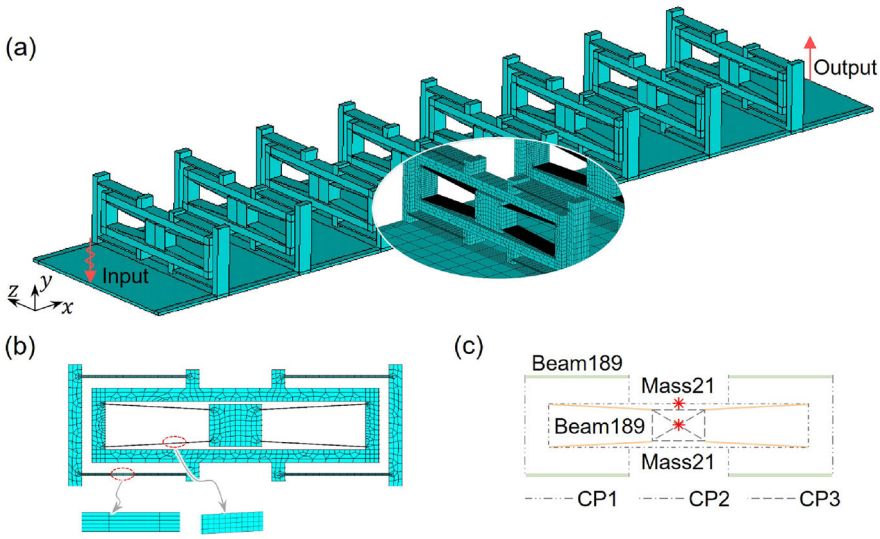

Fig. 6 **a** FE model of finite length NLM beam, **b** Mesh details of attached resonator using Solid185 element type, **c** Simplified FE model of resonator using Beam189 element type and node coupling technique

significantly reduced the number of solid mesh divisions, thus significantly decreasing the calculation time.

We further compared the first two Y-direction vibration modes of the additional resonator modeled with Solid185 element and Beam189 element respectively. As shown in Fig. 7, the deformation modes of the resonator in the first two modes of the two modeling methods are consistent. The motion of m_1 and m_2 is in phase at the 1st mode and antiphase at 2nd mode. Moreover, the modal frequency errors between the two modeling methods are minimal, as listed in Table 2, which also demonstrates the effectiveness of the beam element-dominated modeling method.

Based on the above time-domain nonlinear transient behaviour of the beam element-dominated FE model, the vibration transmission is defined as $T = 20\log|A/A_0|$, where A is the output average amplitude determined by the root-time-square amplitude of the time domain at a specifical frequency. For comparison, a frequency-domain harmonic response analysis was performed to predict the transmissibility characteristics for the linear case.

4.1 Wave transmissibility and verification of the band structures

As shown in Fig. 8a, we compared the wave transmissibility for the linear and nonlinear systems under different excitation amplitudes and the following remarks can be made. First, for the linear case, the band gaps presented in the transmissibility align well

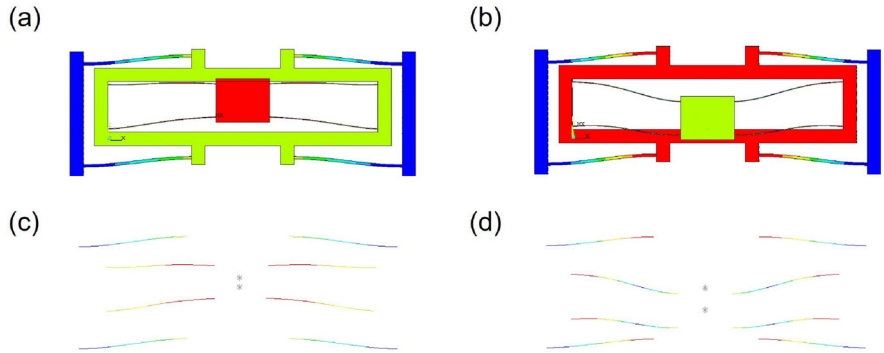

Fig. 7 **a** 1st mode shape of the resonator modeled by Solid185, **b** 2nd mode shape of the resonator modeled by Solid185, **c** 1st mode shape of the resonator modeled by Beam189, **d** 2nd mode shape of the resonator modeled by Beam189. Note that to clearly show the modal shapes, the modal shapes are scaled up, so there is no actual penetrate or contact constraint in the FE simulations

with the predicted one from the imaginary part of the wave vector. Second, for a small excitation amplitude, the nonlinear effect is negligible. Consequently, the comparison between the linear case and the small excitation amplitude shows good agreement. The minor differences observed are primarily due to the use of a linear frequency domain analysis for the linear case and the nonlinear transient analysis for the small excitation amplitude case. Finally, and more importantly, as the excitation amplitude increases, the resonant peak amplitudes are significantly suppressed before the original second linear band gap regions. Additionally, the attenuation region gradually expands to lower frequencies. Specifically, for $A_0 = 0.01$, the three resonant peaks before the second band gap are suppressed. For $A_0 = 0.02$, the four resonant peaks before the second band gap are suppressed. Notably, for $A_0 = 0.03$, the resonant peaks between two original linear bandgaps are suppressed. As a result, the two bandgaps are merged through the nonlinear-induced attenuation region. with a -5 dB threshold, the width of this nonlinear-induced attenuation region is 340% of the original second linear bandgap. Moreover, the frequency boundary of this attenuation region matches well with the predictions from the imaginary part in Fig. 5d.

Table 2 Comparison of modal frequency between two modeling methods

	Modeling by Solid185	Modeling by Beam189	Error
1st mode	164.0	159.3	2.9%
2nd mode	415.9	409.0	1.6%

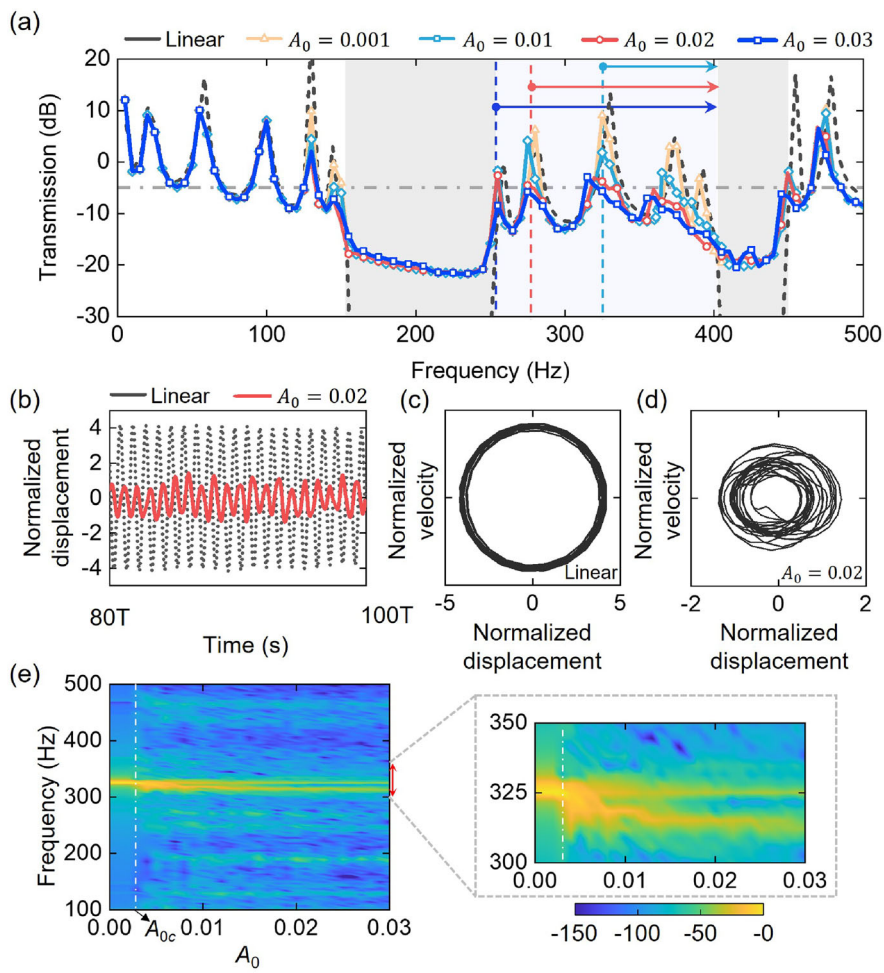

Fig. 8 **a** The wave transmissibility for the linear and nonlinear systems with a varying excitation amplitude; **b** Comparison of the normalized displacements at 325 Hz between the linear case and the nonlinear case with $A_0 = 0.03$; **c–d** Normalized phase diagrams represented by the response trajectories between the normalized displacement and velocity for the linear case and the nonlinear case with $A_0 = 0.03$; (e) Waterfall plot of the power spectrum density (PSD) at the excitation frequency of 325 Hz. The colors correspond to the value $10\log_{10}(\text{PSD})$

Figure 8b shows the comparison of normalized displacement $\widehat{A} = A/A_0$ at 325 Hz between the linear case and the nonlinear case with $A_0 = 0.03$, where significant attenuation is observed compared to the linear case. The corresponding phase diagrams shown in Fig. 8c–d also reveals the linear periodic oscillation and complex nonlinear aperiodic oscillation modes. To further understand the mechanism of this attenuation region, we investigated the influence of the excitation amplitude on the power spectral density of the output response of the measurement point. As shown in Fig. 8e, at 325 Hz, when $A_0 \to 0$, we observe a linear resonance with energy localized at the driving frequency. As A_0 increases beyond a critical value (A_{0c}), energy is no longer localized solely at the driving frequency but disperses over a broad frequency domain. Obviously, a partial enlargement of Fig. 8e reveals another branch of power spectral localization below the driving frequency.

5 Conclusion

This work has been inspired by the fact that the use of nonlinear oscillators in nonlinear metamaterials has been proven to be beneficial for achieving wide bandwidth, but this has been predominantly theoretically and conceptually done with the nonlinearity introduced via discrete spring models, which are not thus convenient for practical realization. To overcome this shortcoming, this study has provided an innovative design of a metastructure involving a mono-slender beam with integrated resonators whose stiffness can be customized to be quasi-linear, hardening, softening or bistable. The additional benefit of the design proposed lies in the fact that a desirable form of nonlinearity in the resonator can be achieved by adjusting only one geometric parameter of the resonator. Thus, each resonator has been constructed to correspond to a serial combination of two nonlinear oscillators, the stiffness of the first one is tailored to be hardening, while the second one is softening. Physical realizations of these oscillators correspond to two block masses attached symmetrically to four beams. In the hardening oscillators, the beams are clamped and initially flat, while their slenderness ratio can be appropriately chosen to achieve a desirable level (strength) of nonlinearity. In the softening oscillators, all four beams are initially oblique, and their configuration has two orthogonal axes of symmetry. One pair of them provides negative stiffness, while the other pair provides approximately linear stiffness; when combined, they yield softening stiffness.

In the next step, the dispersion relation for such infinite-size metastructure has been determined analytically by using the transfer matrix method. The resulting band structure has been found to be amplitude-dependent but widened with respect to the linear counterpart. Additionally, the finite element method has been used to investigate a finite nonlinear metastructure, showing that the nonlinear-induced attenuation region aligns with the predicted bandgap, which is more than three times as wide as the original linear second bandgap. The power spectral density analysis has confirmed that the attenuation is the result of dissipation caused by the interaction between the nonlinear resonators and the host beam.

Acknowledgements This work was supported in part by the National Key Research and Development Program of China under Grant No. 2021YFE0110900, and in part by the National Natural Science Foundation of China (NSFC) under Grants No. U22B2078, and 11991033. The involvement of Ivana Kovacic was supported by the Ministry of Education, Science and Technological Development of the Republic of Serbia via the NOLIMAST project.

Author contributions Jianlei Zhao: Investigation, Methodology, Software, Validation, Writing—original draft, Writing—review & editing. Ivana Kovacic: Validation, Writing –review & editing, Project administration. Rui Zhu: Conceptualization, Supervision, Writing—original draft, Writing—review & editing, Project administration, Funding acquisition.

Funding National Key Research and Development Program of China,2021YFE0110900,2021YFE0110900,2021YFE0110900,National Natural Science Foundation of China,U22B2078,U22B2078

Data availability Relevant data can be made available upon reasonable request.

Declarations

Conflict of interest The authors declare no competing interests.

Appendix A1

For the hardening nonlinear component, the equation of the equivalent single degree of freedom oscillator with a mass m_1, a linear restoring force $k_{h1}y$ and a nonlinear restoring force $k_{h3}y^3$ can be written as follows

$$m_1\ddot{y}_h + c\dot{y}_h + k_{h1}y_h + k_{h3}y_h^3 = -m_1 y_{h0}\omega^2\cos(\omega t) \tag{A1.1}$$

where c, y_{h0}, ω, t are the viscous damping, excitation amplitude, excitation frequency and time, respectively. By introducing the nondimensional variables $\omega_h = \sqrt{k_{h1}/m_1}, \tau = \omega_h t, \Omega_h = \omega/\omega_h, \quad \zeta_h = c/(2m_1\omega_h), \widehat{y}_h = y_h/l, \widehat{y}_{h0} = y_{h0}/l, \quad \alpha_3 = k_{h3}l^2/k_{h1}$, we have the following non-dimensional Duffing equation

$$\widehat{y}_h{}'' + 2\zeta_h\widehat{y}_h{}' + \widehat{y}_h + \alpha_3\widehat{y}_h{}^3 = -\widehat{y}_{h0}\Omega_h{}^2\cos(\Omega_h\tau) \tag{A1.2}$$

where the prime symbol "′" represents the nondimensional time derivative $d/d\tau$.

For weak forcing, damping, nonlinearity, the frequency response equation for this system with cubic Duffing nonlinearity can be determined using the multiple scales method [61]

$$|\widehat{y}_h|^2\left(1-\Omega_h^2+\frac{3}{4}\alpha_3|\widehat{y}_h|^2\right)^2 + (2\zeta\Omega_h|\widehat{y}_h|)^2 = \left(\widehat{y}_{h0}\Omega_h^2\right)^2 \tag{A1.3}$$

The multiple time scales expansion is carried out to second order. The detailed parameters of Fig. 3d are specified as follows: for $\lambda = 0.02$: $\alpha_3 = 846.1$; for $\lambda = 0.04$: $\alpha_3 = 347.6$ and for case $\lambda = 0.06$: $\alpha_3 = 177.0$. The damping ratio $\zeta_h = 0.02$.

Appendix A2

Similarly, for the softening nonlinear component, the equation of the motion of the equivalent single degree of freedom oscillator with a mass m_2, a linear restoring force $k_{s1}y$, a nonlinear restoring force $\sum_{i=2}^{n}k_{si}x^i (n=8)$ can be written as follows

$$|\widehat{y}_h|^2\left(1-\Omega_h^2+\frac{3}{4}\alpha_3|\widehat{y}_h|^2\right)^2 + (2\zeta\Omega_h|\widehat{y}_h|)^2 = \left(\widehat{y}_{h0}\Omega_h^2\right)^2 \tag{A2.1}$$

By introducing the nondimensional variables $\omega_s = \sqrt{k_{s1}/m_2}, \quad \tau = \omega_s t, \quad \Omega_s = \omega/\omega_s, \quad \zeta_s = c/(2m_1\omega_s), \quad \widehat{y}_s = y_s/l, \quad \widehat{y}_{s0} = y_{h0}/l, \quad \alpha_i = k_{si}l^{(i-1)}/k_{s1}$, the following non-dimensional equation is.

$$\widehat{y}_s{}'' + 2\zeta_s\widehat{y}_s{}' + \widehat{y}_s + \sum_{i=2}^{n}\alpha_i\widehat{y}_s{}^i = -\widehat{y}_{s0}\Omega_s{}^2 cos(\Omega_s\tau) \tag{A2.2}$$

For weak forcing, damping, nonlinearity, the frequency response equation for this system with polynomial Duffing nonlinearity can be determined using the multiple scales method [61]

$$|\widehat{y}_s|^2\left(1-\Omega_s^2-\frac{5}{6}\alpha_2^2|\widehat{y}_s|^2+\frac{3}{4}\alpha_3|\widehat{y}_s|^2\right)^2 + (2\zeta_s\Omega_s|\widehat{y}_s|)^2 = \left(\widehat{y}_{s0}\Omega_s^2\right)^2 \tag{A2.3}$$

Higher-order nonlinear terms are approximately ignored in the frequency response due to the second-order multiple time scales expansion. The detailed parameters of Fig. 4d are specified as follows: for $Q = 2$, $\alpha_2 = -7.8\times10^{-14}$ and $\alpha_3 = 4695.3$; for $Q = 4$, $\alpha_2 = -9.6\times10^{-14}$ and $\alpha_3 = 39.8$; for $Q = 6$, $\alpha_2 = -4.8\times10^{-15}$ and $\alpha_3 = -3482.2$; for case $Q = 6$: $\alpha_2 = -8.6\times10^{-14}$ and $\alpha_3 = -7926.5$; The damping ratio $\zeta_h = 0.02$.

Appendix A3

We begin by introducing multiple time scales explicitly as $T_n = \varepsilon^n\tau$ for $n = 0,1,2$. Consequently, the derivative with respect to τ becomes an expansion in terms of the partial derivatives with respect to T_n:

$$\frac{\mathrm{d}}{\mathrm{d}\tau} = \frac{\partial}{\partial T_o} + \varepsilon\frac{\partial}{\partial T_1} + \varepsilon^2\frac{\partial}{\partial T_2} \equiv D_o + \varepsilon D_1 + \varepsilon^2 D_2 \tag{A3.1}$$

We consider the following dimensionless equation of motion with quadratic and cubic nonlinearities:

$$\ddot{\widehat{y}} + \widehat{y} + a_2\widehat{y}^2 + a_3\widehat{y}^3 = 0 \tag{A3.2}$$

The solution to Eq. (A3.2) can be expressed as a series expansion:

$$\widehat{y}(\tau,\varepsilon) = \widehat{y}_0(T_0,T_1,T_2) + \varepsilon\widehat{y}_1(T_0,T_1,T_2) + \varepsilon^2\widehat{y}_2(T_0,T_1,T_2) \tag{A3.3}$$

Substituting Eq. (A3.3) into Eq. (A3.2) and matching the coefficients of powers of ε, we obtain a hierarchy of sub-problems:

$$O(\varepsilon^0) : D_0^2\widehat{y}_0 + \widehat{y}_0 = 0 \tag{A3.4}$$

$$O(\varepsilon^1) : D_0^2\widehat{y}_1 + \widehat{y}_1 = -2D_0D_1\widehat{y}_0 - a_2\widehat{y}_0^2 \tag{A3.5}$$

$$\begin{aligned} O(\varepsilon^2) &: D_0^2\hat{y}_2 + \hat{y}_2 \\ &= -2D_0D_1\hat{y}_1 - 2D_0D_2\hat{y}_0 \\ &\quad -D_1^2\hat{y}_0^2 - 2a_2\hat{y}_0\hat{y}_1 - a_3\hat{y}_0^3 \end{aligned} \tag{A3.6}$$

The solution to Eq. (A3.4) can be conveniently written as:

$$\widehat{y}_0 = Y_0(T_1,T_2)\mathrm{e}^{\mathrm{iT}_0} + cc. \tag{A3.7}$$

where Y_0 is a complex amplitude, and $cc.$ denotes the complex conjugate. Substituting Eq. (A3.7) into Eq. (A3.5), removing secular terms, and set $Y_0 = Y_0(T_2)$, the solution of Eq. (A3.5) is expressed as:

$$\widehat{y}_1 = a_2\left(-Y_0\overline{Y_0} + \frac{1}{3}Y_0^2e^{2iT_0}\right) + cc. \tag{A3.8}$$

Substituting Eq. (A3.7) and Eq. (A3.8) into Eq. (A3.6) and again eliminating secular terms, we derive the non-dimensional frequency response, namely, the frequency modulation equation:

$$\Omega = 1 + \frac{9a_3 + 10a_2^2}{12}Y_0^2 \tag{A3.9}$$

we derive the non-dimensional frequency response, namely, the frequency modulation equation:

$$\ddot{\hat{y}} + (1 + \frac{9a_3 + 10a_2^2}{12}Y_0^2)\hat{y} = 0 \tag{A3.10}$$

Substituting the harmonic solution $\hat{y} = Y_0e^{i\Omega\tau} + cc$ Into Eq. (A3.10), we obtain:

$$-\Omega^2Y_0 + Y_0 + \frac{9a_3 - 10a_2^2}{12}Y_0^3 = 0 \tag{A3.11}$$

Following the procedure above using Eq. (A3.11) for the equivalent system of Eq. (A3.2), we can similarly use the following system of equations as the agent system for Eqs. (10–11):

$$\begin{aligned} &-m_j^1\omega^2\left(W_j(0) + Y_1\right) + k_{\mathrm{h}1}Y_1 - k_{\mathrm{s}1}Y_2 + 3/4k_{\mathrm{h}3}Y_1^3 \\ &\quad + 3/4k_{s3}Y_2^3 - 5/6k_{s2}^2Y_2^3 \\ &\quad = 0 \end{aligned} \tag{A3.12}$$

$$\begin{aligned} &-m_j^2\omega^2\left(W_j(0) + Y_1 + Y_2\right) + k_{\mathrm{s}1}Y_2 + 3/4k_{s3}Y_2^3 \\ &\quad - 5/6k_{s2}^2Y_2^3 \\ &\quad = 0 \end{aligned} \tag{A3.13}$$

Combining Eqs. (A3.12) and (A3.12), we derive Eqs. (14–15).

References

1. Zhu, R., Liu, X.N., Hu, G.K., Sun, C.T., Huang, G.L.: A chiral elastic metamaterial beam for broadband vibration suppression. J. Sound Vib. **333**, 2759–2773 (2014)
2. Chen, Y.Y., Barnhart, M.V., Chen, J.K., Hu, G.K., Sun, C.T., Huang, G.L.: Dissipative elastic metamaterials for broadband wave mitigation at subwavelength scale. Compos. Struct. **136**, 358–371 (2016)
3. Chen, Y., Zheng, M., Liu, X., Bi, Y., Sun, Z., Xiang, P., Yang, J., Hu, G.: Broadband solid cloak for underwater acoustics. Phys. Rev. B **95**, 180104 (2017)
4. Park, J., Youn, J.R., Song, Y.S.: Hydrodynamic metamaterial cloak for drag-free flow. Phys. Rev. Lett. **123**, 74502 (2019)
5. Park, J.J., Park, C.M., Lee, K.J.B., Lee, S.H.: Acoustic superlens using membrane-based metamaterials. Appl. Phys. Lett. **106**, 051901 (2015)
6. Oh, J.H., Min Seung, H., Young Kim, Y.: A truly hyperbolic elastic metamaterial lens. Appl. Phys. Lett. **104**, 73503 (2014)
7. Zhu, R., Liu, X.N., Hu, G.K., Sun, C.T., Huang, G.L.: Negative refraction of elastic waves at the deep-subwavelength scale in a single-phase metamaterial. Nat. Commun. **5**, 1–8 (2014)
8. Andreassen, E., Manktelow, K., Ruzzene, M.: Directional bending wave propagation in periodically perforated plates. J. Sound Vib. **335**, 187–203 (2015)
9. Wang, Y., Zhao, W., Rimoli, J.J., Zhu, R., Hu, G.: Prestress-controlled asymmetric wave propagation and reciprocity-breaking in tensegrity metastructure. Extrem. Mech. Lett. **37**, 100724 (2020)
10. Hu, G., Austin, A.C.M, Sorokin, V., Tang, L.: Metamaterial beam with graded local resonators for broadband vibration suppression. Mech. Syst. Signal Process. **146** 106982 (2021)
11. Miranda Jr, E.J.P., Dos Santos, J.M.C.: Flexural wave band gaps in multi-resonator elastic metamaterial Timoshenko beams. Wave Motion **91**, 102391 (2019)

12. Chaplain, G.J., De Ponti, J.M., Colombi, A., Fuentes-Dominguez, R., Dryburg, P., Pieris, D., Smith, R.J., Clare, A., Clark, M., Craster, R.V.: Tailored elastic surface to body wave Umklapp conversion. Nat. Commun. **11**, 3267 (2020)
13. Chen, Y., Fang, X., Wang, J., Filippi, M., Carrera, E.: An analysis of band gap characteristics of metamaterial plates with dual helix cells. Mech. Adv. Mater. Struct. **31**, 92–102 (2024)
14. Pu, X., Palermo, A., Marzani, A.: Lamb's problem for a half-space coupled to a generic distribution of oscillators at the surface. Int. J. Eng. Sci. **168**, 103547 (2021)
15. Zhang, H., Xiao, Y., Wen, J., Yu, D., Wen, X.: Flexural wave band gaps in metamaterial beams with membrane-type resonators: theory and experiment. J. Phys. D Appl. Phys. **48**, 435305 (2015)
16. Gao, C., Halim, D., Yi, X.: Study of bandgap property of a bilayer membrane-type metamaterial applied on a thin plate. Int. J. Mech. Sci. **184**, 105708 (2020)
17. Lim, C.W.: Elastic waves propagation in thin plate metamaterials and evidence of low frequency pseudo and local resonance bandgaps. Phys. Lett. A **383**, 2789–2796 (2019)
18. Zouari, S., Brocail, J., Génevaux, J.-M.: Flexural wave band gaps in metamaterial plates: A numerical and experimental study from infinite to finite models. J. Sound Vib. **435**, 246–263 (2018)
19. Xue, Y., Li, J., Wang, Y., Li, F.: Tunable nonlinear band gaps in a sandwich-like meta-plate. Nonlinear Dyn. **106**, 2841–2857 (2021)
20. Xiao, Y., Wang, S., Li, Y., Wen, J.: Closed-form bandgap design formulas for beam-type metastructures. Mech. Syst. Signal Process. **159**, 107777 (2021)
21. Wang, Q., Li, J., Zhang, Y., Xue, Y., Li, F.: Bandgap properties in metamaterial sandwich plate with periodically embedded plate-type resonators. Mech. Syst. Signal Process. **151**, 107375 (2021)
22. Jung, J., Goo, S., Wang, S.: Investigation of flexural wave band gaps in a locally resonant metamaterial with plate-like resonators. Wave Motion **93**, 102492 (2020)
23. Zhu, R., Chen, Y.Y., Barnhart, M.V., Hu, G.K., Sun, C.T., Huang, G.L.: Experimental study of an adaptive elastic metamaterial controlled by electric circuits. Appl. Phys. Lett. **108**, 011905 (2016)
24. Yi, K., Collet, M.: Broadening low-frequency bandgaps in locally resonant piezoelectric metamaterials by negative capacitance. J. Sound Vib. **493**, 115837 (2021)
25. Fang, X., Sheng, P., Wen, J., Chen, W., Cheng, L.: A nonlinear metamaterial plate for suppressing vibration and sound radiation. Int. J. Mech. Sci. **228**, 107473 (2022)
26. Narisetti, R.K., Leamy, M.J., Ruzzene, M.: A perturbation approach for predicting wave propagation in one-dimensional nonlinear periodic structures. J. Vib. Acoust. **132**, 031001 (2010)
27. Chakraborty, G., Mallik, A.K.: Dynamics of a weakly nonlinear periodic chain. Int. J. Non. Linear. Mech. **36**, 375–389 (2001)
28. Lazarov, B.S., Jensen, J.S.: Low-frequency band gaps in chains with attached non-linear oscillators. Int. J. Non. Linear. Mech. **42**, 1186–1193 (2007)
29. Bae, M.H., Oh, J.H.: Amplitude-induced bandgap: new type of bandgap for nonlinear elastic metamaterials. J. Mech. Phys. Solids **139**, 103930 (2020)
30. Yang, B., Guo, K., Sun, J.: Towards metamaterial rods with amplitude-dependent band gaps: a superelastic alloy-based approach. Mech. Syst. Signal Process. **166**, 108459 (2022)
31. Luo, B., Gao, S., Liu, J., Mao, Y., Li, Y., Liu, X.: Non-reciprocal wave propagation in one-dimensional nonlinear periodic structures. AIP Adv. **8**, 015113 (2018)
32. Deng, B., Wang, P., He, Q., Tournat, V., Bertoldi, K.: Metamaterials with amplitude gaps for elastic solitons. Nat. Commun. **9**, 3410 (2018)
33. Gao, N., Ma, T., Zhou, W., Wang, Y.-S., Chen, W.: A brief review of solitary waves in nonlinear metamaterials. Mech. Res. Commun. **137**, 104260 (2024)
34. Narisetti, R.K., Leamy, M.J., Ruzzene, M.: A perturbation approach for predicting wave propagation in one-dimensional nonlinear periodic structures. J. Vib. Acoust. Trans. ASME. **132**, 0310011–03100111 (2010)
35. Manktelow, K., Leamy, M.J., Ruzzene, M.: Multiple scales analysis of wave-wave interactions in a cubically nonlinear monoatomic chain. Nonlinear Dyn. **63**, 193–203 (2011)
36. Cveticanin, L., Zukovic, M.: Negative effective mass in acoustic metamaterial with nonlinear mass-in-mass subsystems. Commun. Nonlinear Sci. Numer. Simul. **51**, 89–104 (2017)
37. Yu, M., Fang, X., Yu, D.: Combinational design of linear and nonlinear elastic metamaterials. Int. J. Mech. Sci. **199**, 106422 (2021)
38. Fang, X., Wen, J., Yin, J., Yu, D., Xiao, Y.: Broadband and tunable one-dimensional strongly nonlinear acoustic metamaterials: theoretical study. Phys. Rev. E **94**, 52206 (2016)
39. Shen, Y., Lacarbonara, W.: Nonlinear dispersion properties of metamaterial beams hosting nonlinear resonators and stop band optimization. Mech. Syst. Signal Process. **187**, 109920 (2023)
40. Shen, Y., Lacarbonara, W.: Nonlinearity enhanced wave bandgaps in metamaterial honeycombs embedding spider web-like resonators. J. Sound Vib. **562**, 117821 (2023)
41. Zhao, J., Zhou, H., Yi, K., Kovacic, I., Zhu, R.: Ultra-broad bandgap induced by hybrid hardening and softening nonlinearity in metastructure. Nonlinear Dyn. **111**, 17687–17707 (2023)
42. Casalotti, A., El-Borgi, S., Lacarbonara, W.: Metamaterial beam with embedded nonlinear vibration absorbers. Int. J. Non. Linear. Mech. **98**, 32–42 (2018)
43. Xu, X., Barnhart, M.V., Fang, X., Wen, J., Chen, Y., Huang, G.: A nonlinear dissipative elastic metamaterial for broadband wave mitigation. Int. J. Mech. Sci. **164**, 105159 (2019)
44. Wang, K., Zhou, J., Ouyang, H., Cheng, L., Xu, D.: A semi-active metamaterial beam with electromagnetic quasi-zero-stiffness resonators for ultralow-frequency band gap tuning. Int. J. Mech. Sci. **176**, 105548 (2020)
45. Fang, X., Wen, J., Benisty, H., Yu, D.: Ultrabroad acoustical limiting in nonlinear metamaterials due to adaptive-broadening band-gap effect. Phys. Rev. B **101**, 1–10 (2020)
46. Xia, Y., Ruzzene, M., Erturk, A.: Bistable attachments for wideband nonlinear vibration attenuation in a metamaterial beam. Nonlinear Dyn. **102**, 1285–1296 (2020)
47. Wang, X., Zhang, C., Rui, S., Wu, C., Zhang, W., Ma, F.: Multi-scale material/structure integrated elastic metamaterial for broadband vibration absorbing. Mater. Des. **238**, 112705 (2024)

48. Giri, A.M., Ali, S.F., Arockiarajan, A.: Dynamics of symmetric and asymmetric potential well-based piezoelectric harvesters: a comprehensive review. J. Intell. Mater. Syst. Struct. **32**, 1881–1947 (2021)
49. Yang, T., Zhou, S., Fang, S., Qin, W., Inman, D.J.: Nonlinear vibration energy harvesting and vibration suppression technologies: designs, analysis, and applications. Appl. Phys. Rev. **8**, 031317 (2021)
50. Zhao, J., Zhou, G., Zhang, D., Kovacic, I., Zhu, R., Hu, H.: Integrated design of a lightweight metastructure for broadband vibration isolation. Int. J. Mech. Sci. **244**, 108069 (2023)
51. Liu, C., Zhang, W., Yu, K., Liu, T., Zheng, Y.: Quasi-zero-stiffness vibration isolation: designs, improvements and applications. Eng. Struct. **301**, 117282 (2024)
52. Ledezma-Ramírez, D.F., Tapia-González, P.E., Ferguson, N., Brennan, M., Tang, B.: Recent advances in shock vibration isolation: an overview and future possibilities. Appl. Mech. Rev. **71**, 60802 (2019)
53. Yan, G., Zou, H.-X., Wang, S., Zhao, L.-C., Gao, Q.-H., Tan, T., Zhang, W.-M.: Large stroke quasi-zero stiffness vibration isolator using three-link mechanism. J. Sound Vib. **478**, 115344 (2020)
54. Bian, J., Jing, X.: Analysis and design of a novel and compact X-structured vibration isolation mount (X-Mount) with wider quasi-zero-stiffness range. Nonlinear Dyn. **101**, 2195–2222 (2020)
55. Jing, X., Chai, Y., Chao, X., Bian, J.: In-situ adjustable nonlinear passive stiffness using X-shaped mechanisms. Mech. Syst. Signal Process. **170**, 108267 (2022)
56. Feudo, S. Lo, Touzé, C., Boisson, J., Cumunel, G.: Nonlinear magnetic vibration absorber for passive control of a multi–storey structure. J. Sound Vib. **438**, 33–53 (2019)
57. Mojahed, A., Moore, K., Bergman, L.A., Vakakis, A.F.: Strong geometric softening–hardening nonlinearities in an oscillator composed of linear stiffness and damping elements. Int. J. Non. Linear. Mech. **107**, 94–111 (2018)
58. Fan, X., Mao, X., Dong, Y., Liu, H., Shao, M., Wang, L.: Tunable bandgaps of a metamaterial beam with nonlinear magnetic resonators. Nonlinear Dyn. **112**, 9743–9765 (2024)
59. Shen, Y., Lacarbonara, W.: Wave propagation and multi-stopband behavior of metamaterial lattices with nonlinear locally resonant membranes. Int. J. Non. Linear. Mech. **161**, 104671 (2024)
60. Li, Y.F., Cheng, Y.T., Li, C.L., Song, J. Ben, Liu, Y.Q., Sha, Z.D. Nonlinear pendulum metamaterial to realize an ultra-low-frequency field effect bandgap. Mech. Syst. Signal Process. **223**, 111874 (2025)
61. Zhao, B., Thomsen, H.R., Pu, X., Fang, S., Lai, Z., Damme, B.V., Bergamini, A., Chatzi, E., Colombi, A.: A nonlinear damped metamaterial: Wideband attenuation with nonlinear bandgap and modal dissipation. Mech. Syst. Signal Process. **208**, 111079 (2024)
62. Yu, X., Wang, L.: Nonlinear dynamics of coupled waves in Kresling origami metamaterials. J. Sound Vib. **577**, 118263 (2024)
63. Hajati, A., Kim, S.G.: Ultra-wide bandwidth piezoelectric energy harvesting. Appl. Phys. Lett. (2011).
64. Hajati, A., Kim, S.-G.: Rectifier-less piezoelectric micro power generator. Act. Passiv. Smart Struct. Integr. Syst. **6928**, 521–531 (2008)
65. Dai, X., Miao, X., Sui, L., Zhou, H., Zhao, X., Ding, G.: Tuning of nonlinear vibration via topology variation and its application in energy harvesting. Appl. Phys. Lett. **100**, 031902 (2012)
66. Mettler, E.: Dynamic buckling. In: Flugge (ed.) Handbook of engineering mechanics. McGraw-Hill, New York, (1962)
67. Awtar, S., Sen, S.: A generalized constraint model for two-dimensional beam flexures: Nonlinear load-displacement formulation. J. Mech. Des. **132**, 0810081–08100811 (2010)
68. Ma, F., Chen, G.: Modeling large planar deflections of flexible beams in compliant mechanisms using chained beam-constraint-model. J. Mech. Robot. **8**, 021018 (2016)
69. Nayfeh A H, Mook D T. Nonlinear oscillations[M]. John Wiley & Sons, Hoboken (2008)
70. Fang, X., Lacarbonara, W., Cheng, L.: Advances in nonlinear acoustic/elastic metamaterials and metastructures. Nonlinear Dyn. **4**, 1–28 (2024)
71. Kovacic, I., Brennan, M.J., Lineton, B.: Effect of a static force on the dynamic behaviour of a harmonically excited quasi-zero stiffness system. J. Sound Vib. **325**, 870–883 (2009)

Publisher's Note Springer Nature remains neutral with regard to jurisdictional claims in published maps and institutional affiliations.

Springer Nature or its licensor (e.g. a society or other partner) holds exclusive rights to this article under a publishing agreement with the author(s) or other rightsholder(s); author self-archiving of the accepted manuscript version of this article is solely governed by the terms of such publishing agreement and applicable law.